ACS Energy LETTERS

Cite This: ACS Energy Lett. 2018, 3, 508−513

LETTER

Stable Dopant-Free Asymmetric Heterocontact Silicon Solar Cells with Efficiencies above 20%

James Bullock,[†,‡,#] Yimao Wan,[†,‡,§,#] Zhaoran Xu,[†,‡] Stephanie Essig,[∥] Mark Hettick,[†,‡] Hanchen Wang,[†,‡] Wenbo Ji,[†,‡] Mathieu Boccard,[∥] Andres Cuevas,[§] Christophe Ballif,[∥] and Ali Javey*[,†,‡]

[†]Department of Electrical Engineering and Computer Sciences, University of California, Berkeley, California 94720, United States

[‡]Materials Sciences Division, Lawrence Berkeley National Laboratory, Berkeley, California 94720, United States

[§]Research School of Engineering, The Australian National University (ANU), Canberra, Australian Capital Territory 0200, Australia

[∥]Photovoltaics and Thin Film Electronic Laboratory (PVLab), École Polytechnique Fédérale de Lausanne (EPFL), Institute of Micro Engineering (IMT), Maladière 71b, CH-200 Neuchatel, Switzerland

ABSTRACT: **Development of new device architectures and process technologies is of tremendous interest in crystalline silicon (c-Si) photovoltaics to drive enhanced performance and/or reduced processing cost. In this regard, an emerging concept with a high-efficiency potential is to employ low/high work function metal compounds or organic materials to form asymmetric electron and hole heterocontacts. This Letter demonstrates two important milestones in advancing this burgeoning concept. First, a high-performance, low-temperature, electron-selective heterocontact is developed, comprised of a surface passivating *a*-Si:H layer, a protective TiO_x interlayer, and a low work function LiF_x/Al outer electrode. This is combined with a MoO_x hole-selective heterocontact to demonstrate a cell efficiency of 20.7%, the highest value for this cell class to date. Second, we show that this cell passes a standard stability test by maintaining >95% of its original performance after 1000 h of unencapsulated damp heat exposure, indicating its potential for longevity.**

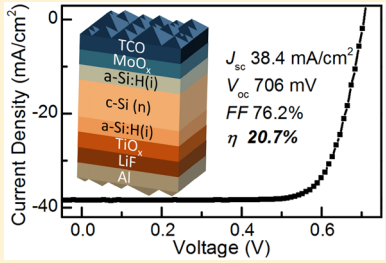

In recent times, there has been a significant increase in the use of metal oxides,[1−6] fluorides,[7−9] sulfides,[10] and organic materials[11,12] as carrier-selective heterocontacts for crystalline silicon (c-Si) photovoltaic (PV) devices. This research stream has been motivated by potential advantages associated with fabrication simplicity and cost reduction. Such materials can be deposited at low temperature (<200 °C) using simple techniques to form full-area heterocontacts with optical characteristics tailored for either the sunward or rear side of a solar cell. These heterocontacts can also overcome or reduce losses common to other c-Si cell architectures (for example, parasitic absorption or heavy impurity doping losses[7,13−15]), increasing the practical efficiency limit of this structure. Most efforts so far have focused on substituting one such heterocontact into an otherwise conventional c-Si cell,[16−20] demonstrating, in many cases, clear performance or fabrication advantages. The ultimate extension of this concept is to use a set of asymmetric heterocontacts in a single cell structure, sometimes referred to as the dopant-free asymmetric heterocontact or DASH cell. In our previous study, we presented a record 19.4% efficient DASH solar cell,[7] utilizing MoO_x- and LiF_x-based heterocontacts with thin amorphous silicon (*a*-Si:H) interfacial passivation layers. Although promising for a first proof-of-concept, it is important to demonstrate that higher conversion efficiencies can be achieved, in line with the suggested higher efficiency potential of this architecture. Further, for a new technology to be considered in a field such as c-Si PV, it must satisfy additional requirements related to thermal steps during cell and module fabrication and to device longevity in operation. Therefore, in this study, the DASH cell structure is revisited with a particular emphasis on simultaneously improving the device efficiency and stability. Modifications to the structure and fabrication allow us to show for the first time that this technology is compatible with efficiencies greater than 20%. We also show that unencapsulated DASH devices can pass an accelerated environmental test designed to simulate the expected damp heat stressors presented to a solar cell over its lifetime.

To increase the DASH cell performance, improvements must be made simultaneously to both the electron and hole heterocontacts. A recent study conducted by coauthors has shown the thermal stability of the hole heterocontact can be improved via an additional annealing step prior to the MoO_x deposition.[21] In this study, we focus on the electron side, aiming to develop a thermally robust rear heterocontact. The electron-selective heterocontact of our first-generation DASH cell utilized a low work function (∼1 nm) LiF_x/Al outer stack to efficiently extract electrons. When applied to c-Si, the low

Received: December 15, 2017
Accepted: January 25, 2018
Published: January 25, 2018

DOI: 10.1021/acsenergylett.7b01279
ACS Energy Lett. 2018, 3, 508−513

work function induces downward band-bending, encouraging electrons to the surface. To improve the stability of this contact, here we integrate thin oxide protective layers to prevent interaction between the thin *a*-Si:H passivation layer and the LiF_x/Al layers, without causing a significant impediment to electron flow. Four candidate oxides are trialled in this application: titanium oxide (TiO_x), tantalum oxide (Ta_2O_x), hafnium oxide (HfO_x), and aluminum oxide (Al_2O_x). All are deposited via atomic layer deposition (ALD) at temperatures ≤ 150 °C (further details can be found in Table 1). These

Table 1. Deposition Conditions and Properties of Atomic-Layer-Deposited Metal Oxide Protective Layers

material	metal precursor	oxidizing precursor	extracted E_g (eV)	oxygen/metal ratio
TiO_x	titanium isopropoxide	water	3.45	2.02
Ta_2O_x	tantalum ethoxide	water	4.4	2.5
HfO_x	tetrakis(diethylamido) hafnium	water	5.65	1.93
Al_2O_x	trimethylaluminum	water	6.08	1.49

materials are chosen to study the influence of conduction band offset on the electron contact performance. To first quantify the conduction band offset, Figure 1 presents the measured optoelectronic properties of TiO_x, Ta_2O_x, HfO_x, and Al_2O_x thin films (~15 nm) deposited on polished c-Si wafers. The work function and valence band spectrum, measured by X-ray photoelectron spectroscopy (XPS), are presented in Figure 1a,b, respectively. The oxygen and metal core levels are also measured by XPS, revealing the stoichiometry of TiO_x (x = 2.02), Ta_2O_x (x = 5.0), HfO_x (x = 1.93), and Al_2O_x (x = 2.98). This is accompanied by the refractive indices (n, k) presented in Figure 1c, extracted from spectroscopic ellipsometry (SE). Implicit within this modeling is a fitting of the optical bandgap E_g, which is included for each oxide in the bottom plot. Combining the extracted E_g with the XPS results in Figure 1a,b allows an estimation of the band positions of these oxides relative to c-Si. As shown in Figure 1d, an increasing conduction band offset can be expected for the four materials, TiO_x < Ta_2O_x < HfO_x < Al_2O_x. The Ta_2O_x and TiO_x films show the lowest conduction band offsets, and hence, they should present the smallest impediment to electron flow.

To test this electrically, TiO_x, Ta_2O_x, HfO_x, and Al_2O_x films of ~3 nm are inserted on the rear side of 2 × 2 cm^2 solar cells with the structure shown in Figure 2a. These cells, referred to here as hybrid cells, utilize a standard silicon heterojunction (SHJ) sunward-side hole contact for simplicity,[22] further details of which can be found in the Methods section. Contrary to our previous studies, a subnanometer layer of LiF_x (~0.6 nm) is used between the metal oxide and Al layers as it was found to provide the lowest resistivities for this heterocontact stack. The PV current density−voltage J−V behavior, measured under standard 1-sun conditions (25 °C, 100 mW/cm^2 AM 1.5G spectrum), is shown in Figure 2b. A clear trend of decreasing fill factor FF due to increasing series resistance R_s is observed, in line with the increasing conduction band offset discussed above. Series resistance values extracted from these J−V curves are included in Figure 2b. The results indicate that, among these materials, TiO_x produces the lowest R_s, likely due to its small conduction band offset with c-Si, and hence, this material is studied in greater detail. The potential of TiO_x for electron extraction/injection has been demonstrated on a number of optoelectronic devices, including solar cells made from a range of absorber materials.[23−25] The use of TiO_x electron heterocontacts in c-Si solar cells has expanded rapidly in recent years, being trialled directly,[12,26] with passivating layers[18,27] and with low work function metals.[16,28] The heterocontact explored here is unique in the combination of passivation, protection, and low work function from the *a*-Si:H, TiO_x, and LiF_x/Al layers. This provides a stable, full-area contact deposited via simple means with high rear-reflection. Figure 2c shows J−V curves measured on hybrid cells with different TiO_x thicknesses ranging from 6 to 1.5 nm. The three solid lines correspond to the J−V curves of cells cut from the same wafer and processed in parallel, showing that the thinnest film of 1.5 nm exhibits the smallest series resistance. Thinner films were not trialled due to the likelihood of incomplete surface coverage, and cells made without any TiO_x (not shown) had lower open-circuit voltage V_{oc} and FF values than those with the 1.5 nm TiO_x film. The dotted line represents the best of five devices measured on a full (uncut) wafer processed using the same *a*-Si:H/TiO_x (1.5 nm)/LiF_x (~0.6 nm)/Al rear electron contact. This hybrid cell reaches an efficiency of 20.9%, supported by a V_{oc} of 713 mV and a FF of 78.1%.

As discussed above, the primary role of the TiO_x interlayer is to improve the stability of the device. To investigate this effect, a set of four transfer-length-method (TLM) samples was prepared on n-type c-Si (1 Ω·cm) for the extraction of contact resistivity ρ_c. These four test samples were fabricated with the following contact stacks: (i) *a*-Si:H/TiO_x (1.5 nm)/LiF_x (~0.6 nm)/Al; (ii) *a*-Si:H/LiF_x (~0.6 nm)/Al; (iii) TiO_x (1.5 nm)/LiF_x (~0.6 nm)/Al; and (iv) LiF_x (~0.6 nm)/Al. Figure 3a shows the measured ρ_c of the four samples as a function of annealing temperature in air. The measurements were taken

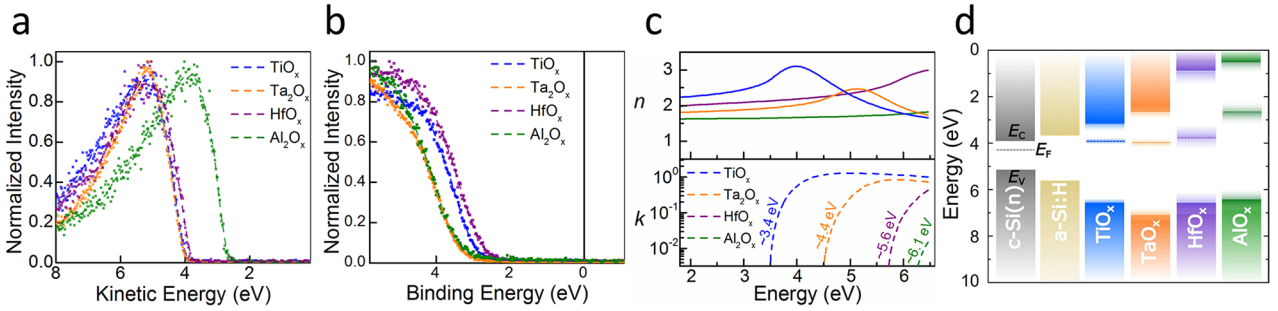

Figure 1. | Electron contact materials. (a) Secondary electron cutoff energy (for work function), (b) valence band spectrum, and (c) refractive indices (top: real part n; bottom: imaginary part k) of different metal oxide protective films. (d) Potential band position diagram for the electron heterocontact materials using information from (a−c).

DOI: 10.1021/acsenergylett.7b01279
ACS Energy Lett. 2018, 3, 508−513

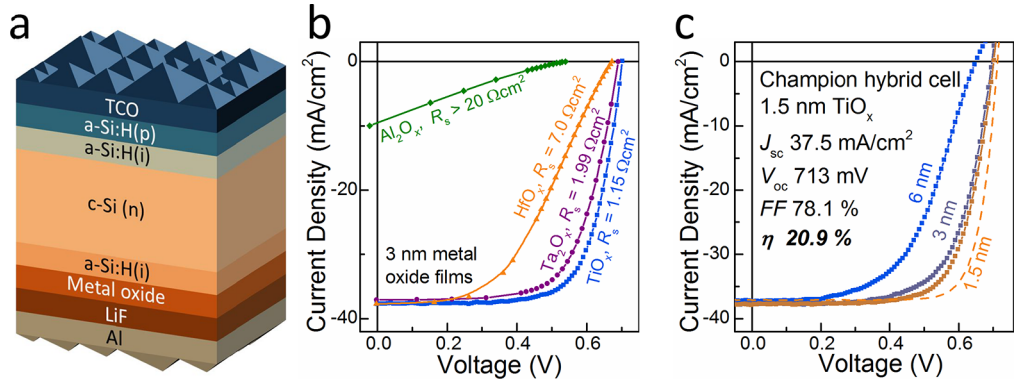

Figure 2. | Electron contact optimization. (a) Structure of the hybrid cell used for contact optimization, (b) 1-sun light *J*−*V* behavior of hybrid cells with 3 nm protective metal oxide layers, (c) 1-sun light *J*−*V* behavior of hybrid cells with different TiO_x thicknesses showing an optimum thickness of 1.5 nm.

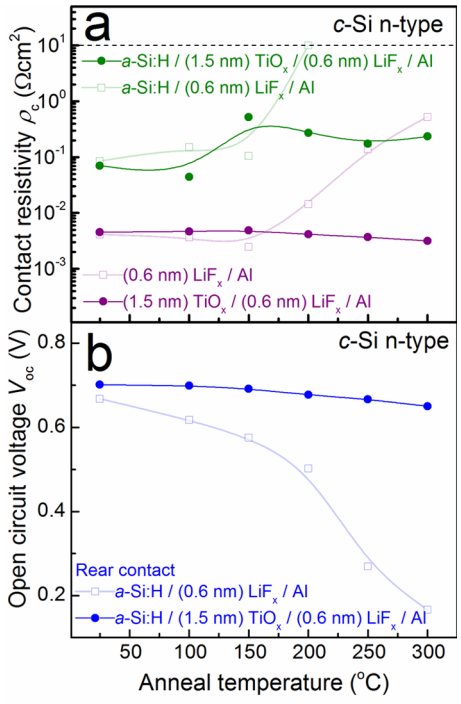

Figure 3. | Electron contact stability. (a) ρ_c as a function of sequential 10 min anneals at increasing temperatures for samples with/without *a*-Si:H and TiO_x layers. (b) V_{oc} progression of hybrid cells after sequential 10 min anneals at increasing temperatures for cells with/without the TiO_x layer.

after successive 10 min anneals at incrementally increasing temperatures between room temperature and 300 °C; hence, the last point corresponds to a cumulative annealing time of 50 min. It can be seen that the addition of the 1.5 nm TiO_x layer does not increase the as-deposited ρ_c. This is true for both contacts with and without the *a*-Si:H layers with ρ_c values of ∼70 and 4 mΩ·cm², respectively. More importantly, the TiO_x layer improves the thermal stability of ρ_c drastically for annealing temperatures up to 300 °C. It should be noted that TLM samples fabricated without the LiF_x interlayer (not shown) exhibited significantly higher ρ_c values than those shown in Figure 3a.

A second stability test, conducted on two hybrid solar cells with and without a 1.5 nm TiO_x layer, is presented in Figure 3b. Whereas the V_{oc} of the cell without TiO_x degrades drastically as the annealing temperature increases, a significant improvement in the passivation stability is achieved as a result of the TiO_x interlayer addition. The enhanced stability results presented in Figure 3a for the ρ_c and in Figure 3b for the V_{oc} are likely due to the prevention of intermixing between the *a*-Si:H and the LiF_x/Al layers. TiO_x protective layers have been utilized in a number of silicon-based structures, including photoelectrochemical cells as a protective film in harsh chemical environments[29] and in microelectronics and solar cell devices as a high-temperature diffusion barrier to metals and dopants.[30,31] Without this layer, at elevated temperatures, the angstrom-scale LiF_x (∼0.6 nm) may not provide sufficient protection of the thin *a*-Si:H passivation layer from the overlying Al layer. A number of studies have shown metal-induced crystallization of *a*-Si:H at low temperatures upon contact with Al,[32−34] a process that will increase interface recombination.

Finally, the optimized *a*-Si:H/TiO_x/LiF_x/Al electron heterocontact is combined with a front, *a*-Si:H/MoO_x/indium tin oxide (ITO) hole heterocontact into a full 2 × 2 cm² DASH cell with the structure shown in Figure 4a. The front MoO_x heterocontact fabrication is conducted in line with the suggestions of ref 21 to improve its thermal stability. The 1-sun *J*−*V* results of the stability-enhanced DASH is provided in Figure 4b, showing that a conversion efficiency of 20.7% has been achieved, supported by a V_{oc} of 706 mV and a FF of 76.2%. This is the first demonstration of a DASH cell above 20%. A quantum efficiency analysis of this cell is also included in Figure 4c, showing the measured external quantum efficiency (EQE), reflection, and internal quantum efficiency (IQE), taken in-between Ag metal grid fingers. After accounting for a contact fraction of ∼3%, the integration of the EQE and the solar spectrum product gives a J_{sc} of 38.8 mA/cm². This value agrees well with that obtained directly from the light *J*−*V* of 38.4 mA/cm² supporting the accuracy of the value. To further test the stability of the electron and hole contact structures, a representative unencapsulated DASH cell is subjected to a standard 1000 h damp heat test at 85 °C and 85% relative humidity (RH). Table 2 shows the measured characteristic parameters of this device before and after the 1000 h period, revealing that 96% of the original performance has been maintained.

In this Letter, we have simultaneously improved the benchmark efficiency and stability of c-Si DASH solar cells. We have found that the thermal stability of the electron-

DOI: 10.1021/acsenergylett.7b01279
ACS Energy Lett. 2018, 3, 508−513

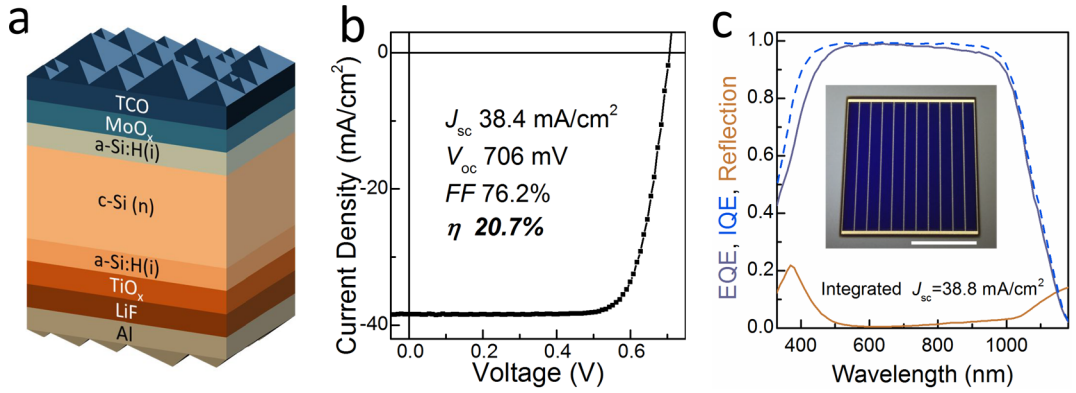

Figure 4. | DASH cell record. (a) Structure of the DASH cell, (b) 1-sun light *J*–*V* behavior of the champion DASH cell, (c) external quantum efficiency (EQE), internal quantum efficiency (IQE), and reflection of the champion DASH cell; the inset shows a photograph of the cell design and the integrated J_{sc} value. The white scale bar is ~1 cm.

Table 2. Damp Heat Stability with 1-sun *J*–*V* Characteristics of a Representative DASH Cell Measured before and after 1000 h of Unencapsulated Exposure to 85 °C and 85% RH

	V_{oc} (mV)	FF (%)	J_{sc} (mA/cm^2)	η (%)
as-fabricated	698	73.5	38.2	19.6
1000 h at 85 °C, 85% RH	696	71.3	38.2	19.0

selective heterocontacts can be improved by introducing a protective TiO_x interlayer between the *a*-Si:H passivation layer and the low work function LiF_x/Al electrode. This second-generation DASH cell has been proven to maintain >95% of its performance after 1000 h of unencapsulated damp heat exposure. Importantly, the improved stability does not come at the expense of performance. On the contrary, a conversion efficiency of 20.7% has been demonstrated, the highest value of any DASH solar cell presented to date. These developments in efficiency and stability pave the way for the DASH cell design to become a viable contender for high-performance, low-cost c-Si PV.

METHODS

Materials Characterization. Samples for XPS and SE were fabricated by depositing thin films of TiO_x, Ta_2O_x, HfO_x, and Al_2O_x on a polished n^+ silicon wafer, which was given a short 5% HF etch prior to deposition. The thin films were deposited by ALD, with a chamber temperature of ≤150 °C. Further details can be found in Table 1. XPS measurements were performed in a Kratos spectrometer with an Al monochromatic X-ray source. All measurements were performed on thin films (~15 nm) without electron gun neutralization. Charging is known to be a general issue in XPS, particularly for insulating films. Efforts were made to minimize charging by reducing incident X-ray exposure during the secondary electron cutoff measurement, and core level and valence band spectra were referenced to a C 1s peak at 284.8 eV. For the secondary electron cutoff measurement, a sputter-cleaned Au sample was included in each run as a reference. The ranges provided for the Fermi energy, conduction band, and valence band of each material in the schematic of Figure 1d are based off of the measured variation in XPS results. SE measurements were also taken on ~15 nm films with a JA Wollam M 2000 spectroscopic ellipsometer, and the films were fitted with Tauc–Lorentz models, the optical bandgaps of which are listed in Table 1.

Device Fabrication and Characterization. Contact structures were fabricated according to a TLM design. Samples with and without the thin (~5 nm) *a*-Si:H passivation layer were deposited on 4 and 1 Ω·cm n-type float zone (FZ) wafers, respectively. The *a*-Si:H was deposited via plasma-enhanced chemical vapor deposition (PECVD). Half of these received a thin 1.5 nm TiO_x protective layer following which they were all deposited with a LiF_x (0.6 nm)/Al electrode through a shadow mask to achieve the TLM pattern. The dark current–voltage *I*–*V* behavior was measured as a function of pad spacing using a Keithley 2400 sourcemeter, and the contact resistivity was extracted from this relationship according to ref 35. Annealing of contact samples was performed on a hot plate in air at temperatures between 100 and 300 °C.

The hybrid cell structures utilized in Figures 2 and 3 were fabricated on double-side textured, FZ, 4 Ω·cm n-type wafers with a thickness of ~250 μm. The front hole heterocontact consisted of a stack of intrinsic (~5 nm) and boron-doped (~10 nm) *a*-Si:H layers. This was capped with an indium tin oxide (ITO) layer that was sputtered through a shadow mask to define a 2 × 2 cm^2 area. The *a*-Si:H layers were deposited via PECVD and the TCOs via DC sputtering. The front Ag grid, with a surface fraction of ~3%, was achieved by screen printing a low-temperature Ag paste and curing. For the rear contact, an intrinsic thin *a*-Si:H layer (~5 nm) was coated with either TiO_x, Ta_2O_x, HfO_x, or Al_2O_x thin films deposited via ALD using the precursors listed in Table 1. These were capped with a low work function LiF_x (~0.6 nm)/Al (~200 nm) electrode deposited via thermal evaporation. Hybrid cell annealing was performed in a quartz tube furnace between 100 and 300 °C.

The 2 × 2 cm^2 DASH cell was also fabricated on a double-side textured 4 Ω·cm n-type wafer with a thin (~5 nm) passivating *a*-Si:H layer on either side. This was subjected to a short anneal at 250 °C prior to contact deposition, in line with the suggestions of ref 21. Next, the front side was deposited with ~5 nm of thermally evaporated MoO_x followed by ~70 nm of sputtered ITO, and finally, low-temperature Ag paste was screen printed and cured at 190 °C. The rear side was deposited with 1.5 nm of ALD TiO_x followed by the thermally evaporated LiF_x (~0.6 nm)/Al electrode.

A 1-sun *J*–*V* analysis of these cells was performed under standard conditions (25 °C, 100 mW/cm^2, AM 1.5G spectrum) using a calibrated solar simulator and an aperture mask to avoid peripheral absorption. The EQE and reflection were measured in an in-house built setup. An Espec LHU humidity chamber,

DOI: 10.1021/acsenergylett.7b01279
ACS Energy Lett. 2018, 3, 508–513

held at 85 °C and 85% RH, was used for the humidity exposure test.

AUTHOR INFORMATION

Corresponding Author

*E-mail: ajavey@berkeley.edu.

ORCID

James Bullock: 0000-0001-7903-9642

Yimao Wan: 0000-0003-2999-2464

Ali Javey: 0000-0001-7214-7931

Author Contributions

#J.B. and Y.W. contributed equally to this work.

Notes

The authors declare no competing financial interest.

ACKNOWLEDGMENTS

Device design, fabrication, and characterization at Berkeley were funded by the U.S. Department of Energy, Solar Energy Technologies Office. Materials characterization was supported by the Electronic Materials Programs, funded by the Director, Office of Science, Office of Basic Energy Sciences, Material Sciences and Engineering Division of the U.S. Department of Energy under Contract No. DE-AC02-05CH11231. XPS characterization was performed at the Joint Center for Artificial Photosynthesis, supported through the Office of Science of the U.S. Department of Energy under Award Number DE-SC0004993. Work at the Molecular Foundry was supported by the Office of Science, Office of Basic Energy Sciences, of the U.S. Department of Energy (Contract No. DE-AC02-05CH11231). S.E. held a Marie Skłodowska-Curie Individual Fellowship from the European Research Council (ERC) under the European Union's Horizon 2020 research and innovation programme (Grant Agreement No: 706744, action acronym: COLIBRI). Work at EPFL was financially supported by the Swiss National Science Foundation via the NRP70 "Energy Turnaround" Project "PV2050". Work at the ANU was supported by the Australian Government through the Australian Research Council (Discovery Project: DP150104331) and the Australia–US Institute for Advanced Photovoltaics (AUSIAPV) program under Grant Number ACAP6.9.

REFERENCES

(1) Battaglia, C.; Yin, X.; Zheng, M.; Sharp, I. D.; Chen, T.; McDonnell, S.; Azcatl, A.; Carraro, C.; Ma, B.; Maboudian, R.; et al. Hole Selective MoO_x Contact for Silicon Solar Cells. *Nano Lett.* **2014**, *14*, 967–971.

(2) Avasthi, S.; McClain, W. E.; Man, G.; Kahn, A.; Schwartz, J.; Sturm, J. C. Hole-Blocking Titanium-Oxide/Silicon Heterojunction and Its Application to Photovoltaics. *Appl. Phys. Lett.* **2013**, *102*, 203901.

(3) Wan, Y.; Samundsett, C.; Bullock, J.; Hettick, M.; Allen, T.; Yan, D.; Peng, J.; Wu, Y.; Cui, J.; Javey, A.; et al. Conductive and Stable Magnesium Oxide Electron-Selective Contacts for Efficient Silicon Solar Cells. *Adv. Energy Mater.* **2017**, *7*, 1601863.

(4) Bivour, M.; Temmler, J.; Steinkemper, H.; Hermle, M. Molybdenum and Tungsten Oxide: High Work Function Wide Band Gap Contact Materials for Hole Selective Contacts of Silicon Solar Cells. *Sol. Energy Mater. Sol. Cells* **2015**, *142*, 34–41.

(5) Gerling, L. G.; Mahato, S.; Morales-Vilches, A.; Masmitja, G.; Ortega, P.; Voz, C.; Alcubilla, R.; Puigdollers, J. Transition Metal Oxides as Hole-Selective Contacts in Silicon Heterojunctions Solar Cells. *Sol. Energy Mater. Sol. Cells* **2016**, *145*, 109–115.

(6) Macco, B.; Vos, M. F. J.; Thissen, N. F. W.; Bol, A. A.; Kessels, W. M. M. Low-Temperature Atomic Layer Deposition of MoO_x for Silicon Heterojunction Solar Cells. *Phys. Status Solidi RRL* **2015**, *9*, 393–396.

(7) Bullock, J.; Hettick, M.; Geissbühler, J.; Ong, A. J.; Allen, T.; Sutter-Fella, C. M.; Chen, T.; Ota, H.; Schaler, E. W.; De Wolf, S.; et al. Efficient Silicon Solar Cells with Dopant-Free Asymmetric Heterocontacts. *Nat. Energy* **2016**, *1*, 15031.

(8) Wan, Y.; Samundsett, C.; Bullock, J.; Allen, T.; Hettick, M.; Yan, D.; Zheng, P.; Zhang, X.; Cui, J.; McKeon, J.; et al. Magnesium Fluoride Electron-Selective Contacts for Crystalline Silicon Solar Cells. *ACS Appl. Mater. Interfaces* **2016**, *8*, 14671–14677.

(9) Zhang, Y.; Liu, R.; Lee, S.-T.; Sun, B. The Role of a LiF Layer on the Performance of Poly(3,4-Ethylenedioxythiophene):Poly-(Styrenesulfonate)/Si Organic-Inorganic Hybrid Solar Cells. *Appl. Phys. Lett.* **2014**, *104*, 083514.

(10) Xu, X.; Bullock, J.; Schelhas, L. T.; Stutz, E. Z.; Fonseca, J. J.; Hettick, M.; Pool, V. L.; Tai, K. F.; Toney, M. F.; Fang, X.; et al. Chemical Bath Deposition of P-Type Transparent, Highly Conducting $(CuS)_x$:$(ZnS)_{1-x}$ Nanocomposite Thin Films and Fabrication of Si Heterojunction Solar Cells. *Nano Lett.* **2016**, *16*, 1925–1932.

(11) Zielke, D.; Pazidis, A.; Werner, F.; Schmidt, J. Organic-Silicon Heterojunction Solar Cells on n-Type Silicon Wafers: The Back-PEDOT Concept. *Sol. Energy Mater. Sol. Cells* **2014**, *131*, 110–116.

(12) Nagamatsu, K. A.; Avasthi, S.; Sahasrabudhe, G.; Man, G.; Jhaveri, J.; Berg, A. H.; Schwartz, J.; Kahn, A.; Wagner, S.; Sturm, J. C. Titanium Dioxide/Silicon Hole-Blocking Selective Contact to Enable Double-Heterojunction Crystalline Silicon-Based Solar Cell. *Appl. Phys. Lett.* **2015**, *106*, 123906.

(13) Holman, Z. C.; Descoeudres, A.; Barraud, L.; Fernandez, F. Z.; Seif, J. P.; De Wolf, S.; Ballif, C. Current Losses at the Front of Silicon Heterojunction Solar Cells. *Photovolt. IEEE J. Of* **2012**, *2*, 7–15.

(14) Richter, A.; Glunz, S. W.; Werner, F.; Schmidt, J.; Cuevas, A. Improved Quantitative Description of Auger Recombination in Crystalline Silicon. *Phys. Rev. B: Condens. Matter Mater. Phys.* **2012**, *86*, 165202.

(15) Battaglia, C.; de Nicolas, S. M.; De Wolf, S.; Yin, X.; Zheng, M.; Ballif, C.; Javey, A. Silicon Heterojunction Solar Cell with Passivated Hole Selective MoO_x Contact. *Appl. Phys. Lett.* **2014**, *104*, 113902.

(16) Allen, T. G.; Bullock, J.; Jeangros, Q.; Samundsett, C.; Wan, Y.; Cui, J.; Hessler-Wyser, A.; De Wolf, S.; Javey, A.; Cuevas, A. A Low Resistance Calcium/Reduced Titania Passivated Contact for High Efficiency Crystalline Silicon Solar Cells. *Adv. Energy Mater.* **2017**, *7*, 1602606.

(17) Bullock, J.; Zheng, P.; Jeangros, Q.; Tosun, M.; Hettick, M.; Sutter-Fella, C. M.; Wan, Y.; Allen, T.; Yan, D.; Macdonald, D.; et al. Lithium Fluoride Based Electron Contacts for High Efficiency N-Type Crystalline Silicon Solar Cells. *Adv. Energy Mater.* **2016**, *6*, 1600241.

(18) Yang, X.; Weber, K.; Hameiri, Z.; De Wolf, S. Industrially Feasible, Dopant-Free, Carrier-Selective Contacts for High-Efficiency Silicon Solar Cells. *Prog. Photovoltaics* **2017**, *25*, 896–904.

(19) Masmitjà, G.; Gerling, L. G.; Ortega, P.; Puigdollers, J.; Martín, I.; Voz, C.; Alcubilla, R. V_2O_x-Based Hole-Selective Contacts for c-Si Interdigitated Back-Contacted Solar Cells. *J. Mater. Chem. A* **2017**, *5*, 9182–9189.

(20) Geissbühler, J.; Werner, J.; Martin de Nicolas, S.; Barraud, L.; Hessler-Wyser, A.; Despeisse, M.; Nicolay, S.; Tomasi, A.; Niesen, B.; De Wolf, S.; et al. 22.5% Efficient Silicon Heterojunction Solar Cell with Molybdenum Oxide Hole Collector. *Appl. Phys. Lett.* **2015**, *107*, 081601.

(21) Essig, S.; Dréon, J.; Rucavado, E.; Mews, M.; Koida, T.; Boccard, M.; Werner, J.; Geissbuhler, J.; Löper, P.; Morales-Masis, M.; et al. Towards Annealing-Stable Molybdenum-Oxide-Based Hole-Selective Contacts for Si Photovoltaics. *Sol. Rapid Res. Lett.* **2018**, Accepted.

(22) Descoeudres, A.; Holman, Z. C.; Barraud, L.; Morel, S.; De Wolf, S.; Ballif, C. >21%; Efficient Silicon Heterojunction Solar Cells on n- and p-Type Wafers Compared. *Photovolt. IEEE J. Of* **2013**, *3*, 83–89.

DOI: 10.1021/acsenergylett.7b01279
ACS Energy Lett. 2018, 3, 508–513

(23) Liu, M.; Johnston, M. B.; Snaith, H. J. Efficient Planar Heterojunction Perovskite Solar Cells by Vapour Deposition. *Nature* **2013**, *501*, 395.
(24) Hsu, W.; Sutter-Fella, C. M.; Hettick, M.; Cheng, L.; Chan, S.; Chen, Y.; Zeng, Y.; Zheng, M.; Wang, H.-P.; Chiang, C.-C.; et al. Electron-Selective TiO_2 Contact for $Cu(In,Ga)Se_2$ Solar Cells. *Sci. Rep.* **2015**, *5*, 16028.
(25) Yin, X.; Battaglia, C.; Lin, Y.; Chen, K.; Hettick, M.; Zheng, M.; Chen, C.-Y.; Kiriya, D.; Javey, A. 19.2% Efficient InP Heterojunction Solar Cell with Electron-Selective TiO_2 Contact. *ACS Photonics* **2014**, *1*, 1245−1250.
(26) Boccard, M.; Yang, X.; Weber, K.; Holman, Z. C. Passivation and Carrier Selectivity of TiO_2 Contacts Combined with Different Passivation Layers and Electrodes for Silicon Solar Cells. *2016 IEEE 43rd Photovoltaic Specialists Conference (PVSC)* **2016**, 2403−2407.
(27) Cho, J.; Debucquoy, M.; Recaman Payo, M.; Malik, S.; Filipič, M.; Radhakrishnan, H. S.; Bearda, T.; Gordon, I.; Szlufcik, J.; Poortmans, J. Contact Resistivity Reduction on Lowly-Doped n-Type Si Using a Low Workfunction Metal and a Thin TiO_x Interfacial Layer for Doping-Free Si Solar Cells. *Energy Procedia* **2017**, *124*, 842−850.
(28) Bullock, J.; Ota, H.; Wang, H.; Xu, Z.; Essig, S.; Samundsett, C.; Yan, D.; Hettick, M.; Morales-Masis, M.; Wan, Y.; et al. Microchannel Contacting of Crystalline Silicon Solar Cells. *Sci. Rep.* **2017**, *7*, 9085.
(29) Bae, D.; Seger, B.; Vesborg, P. C. K.; Hansen, O.; Chorkendorff, I. Strategies for Stable Water Splitting via Protected Photoelectrodes. *Chem. Soc. Rev.* **2017**, *46*, 1933−1954.
(30) Richards, B. S.; Richards, S. R.; Boreland, M. B.; Jamieson, D. N. High Temperature Processing of TiO_2 Thin Films for Application in Silicon Solar Cells. *J. Vac. Sci. Technol., A* **2004**, *22*, 339−348.
(31) Alén, P.; Vehkamäki, M.; Ritala, M.; Leskelä, M. Diffusion Barrier Properties of Atomic Layer Deposited Ultrathin Ta_2O_5 and TiO_2 Films. *J. Electrochem. Soc.* **2006**, *153*, G304−G308.
(32) Plagwitz, H.; Nerding, M.; Ott, N.; Strunk, H. P.; Brendel, R. Low-Temperature Formation of Local Al Contacts to a-Si:H-Passivated Si Wafers. *Prog. Photovoltaics* **2004**, *12*, 47−54.
(33) Bullock, J.; Yan, D.; Wan, Y.; Cuevas, A.; Demaurex, B.; Hessler-Wyser, A.; De Wolf, S. Amorphous Silicon Passivated Contacts for Diffused Junction Silicon Solar Cells. *J. Appl. Phys.* **2014**, *115*, 163703.
(34) Bullock, J.; Cuevas, A.; Yan, D.; Demaurex, B.; Hessler-Wyser, A.; De Wolf, S. Amorphous Silicon Enhanced Metal-Insulator-Semiconductor Contacts for Silicon Solar Cells. *J. Appl. Phys.* **2014**, *116*, 163706.
(35) Schroder, D. K. *Semiconductor Material and Device Characterization*, 3rd ed.; John Wiley & Sons: Hoboken, NJ, 2006; pp 389−465.

DOI: 10.1021/acsenergylett.7b01279
ACS Energy Lett. 2018, 3, 508−513